X International Conference on Computational Methods for Coupled Problems in Science and Engineering
COUPLED PROBLEMS 2023
M. Papadrakakis, B. Schrefler and E. Oñate (Eds)

MULTIPHYSICAL MODELING OF SOFT TISSUE-STENT INTERACTION

Stefanie Reese*, Kiran Manjunatha*, Jianye Shi* and Mahmoud Sesa*

*Institute of Applied Mechanics, RWTH Aachen University
Mies-van-der-Rohe-Str. 1, D-52074 Aachen, Germany
e-mail: stefanie.reese@ifam.rwth-aachen.de, web page: https://www.ifam.rwth-aachen.de/

Key words: multiphysics, in-stent restenosis, drug-eluting stents, continuum growth modeling, finite element technologies, physics-informed neural networks

Abstract. The prevalence of in-stent restenosis after percutaneous coronary intervention necessitates the development of computational tools to derive pathophysiological inferences and fine-tune interventional procedures patient-specifically. In this context, a multiphysics framework is presented herein that captures the chemo-mechano-biological interaction involved. Strategies that could potentially accelerate the computations as well as add versatility to them are shortly discussed. We hence take a minute step towards enabling computer-assisted clinical practices.

1 Introduction

Given the unhealthy lifestyle of the majority of the current population, which involves the consumption of extensively processed foods, sedentary habits, and smoking to name a few, the occurrence of cardiovascular diseases is exacerbated. Coronary artery disease (CAD), wherein the extensive amount of plaque built up in the coronary arteries leads to ischemic events, and in extreme cases myocardial infarction, is hence one of the leading causes of mortality globally. Percutaneous coronary intervention (PCI) and subsequent implantation of scaffolds called stents is the most prevalent option to alleviate the symptoms of CAD by restoring healthy blood flow in the blocked coronary arteries. But PCI and stent implantation are associated with the risks of two major unexpected outcomes: (1) stent thrombosis (ST) and (2) in-stent restenosis (ISR).

Within this work, we focus on the latter outcome, ISR. Friction between the PCI balloon or the stent and the arterial wall, in addition to the arterial overstretch achieved during PCI, leads to more or less complete denudation of the endothelial monolayer. The endothelium acts as a barrier preventing the exposure of subendothelial contents to the blood flow. The denudation of this layer then leads to the exposition of extracellular contents to the blood flow kickstarting a cascade of inflammatory responses. These include aggregation of platelets, the release of cytokines and mitogenic agents into the subendothelial space that result in migration and proliferation of smooth muscle cells (SMCs), infiltration of circulating monocytes, etc. This then leads to uncontrolled growth of the tissue resulting in the recurrence of obstruction to blood flow thereby defeating the purpose of PCI. The mechanism involved herein is termed neointimal hyperplasia. Although modern drug-eluting stents (DESs) have been able to reduce the prevalence of ISR to a great extent, the issue still persists owing to the patient specificity of the

inflammatory responses and the inability of clinical infrastructure to tune the PCI procedures accordingly.

Several computational models have been proposed to model ISR. They can be largely classified into: **(a)** cellular automata (CA) + agent-based modeling (ABM) approaches - see [1], [2], [3], and [4] **(b)** phenomenological continuum mechanical models - see [5], [6], and [7], and **(c)** multiscale multiphysics-based chemo-mechano-biological continuum models - see [8] and [9].

Computational models that incorporate the influence of pharmacokinetics and pharmacokinetics pertaining to drugs embedded in DESs have been scarce in the literature. [10], [11], and [12] are the few works which deal with the aforementioned aspects. The current work hence serves as a contribution toward the development of computational methods that model ISR considering the complex interplay between significant mediators and drug-elution kinetics with a considerable resolution that can help derive insights and adapt interventional procedures.

2 Overview

As part of the priority programme "*SPP 2311: Robust coupling of continuum-biomechanical in silico models to establish active biological system models for later use in clinical applications - Co-design of modeling, numerics and usability*", funded by the German Research Foundation (DFG), our project aims to advance the implementation of *in silico* tools that can be utilized in clinical practice. Specifically, the project focuses on the identification and modeling of the behaviors of significant mediators of neointimal hyperplasia, a post-operative complication occurring in patients undergoing PCI. The complex biochemical interactions that constitute the inflammatory response of the coronary artery are to be modeled by setting up a coupled multiphysics framework, which then serves as a tool to improve stent designs, steer the pharmacokinetics from current generation DESs, and finally optimize the interventional parameters patient-specifically.

Through the following sections, we aim to introduce our modeling framework by first elaborating on the continuum growth modeling. Further, an overview of the balance equations that govern the behaviors of the key mediators of ISR is presented. Numerical investigations that probe the framework are then discussed, strategies to improve the computational efficiency of the modeling framework are proposed, and in conclusion, a brief outlook is provided.

2.1 Continuum mechanical modeling

The arterial wall is assumed to be composed of two layers, the media and the adventitia, each consisting of two helices of collagen fibres embedded in an isotropic ground matrix. To model the volumetric growth involved in the restenotic process, we adopt the well-known multiplicative split of the deformation gradient $\boldsymbol{F}$ [13], i.e.,

$$\boldsymbol{F} = \boldsymbol{F}_e \, \boldsymbol{F}_g, \tag{1}$$

where $\boldsymbol{F}_g$ maps the referential geometry to an intermediate stress-free grown state, while $\boldsymbol{F}_e$ achieves the compatibility of deformations. Upon further decomposition of the growth part $\boldsymbol{F}_g$ into a pure stretch part and a pure rotational part [14], i.e.,

$$\boldsymbol{F}_g = \boldsymbol{R}_g \, \boldsymbol{U}_g, \tag{2}$$

we can rewrite the decomposition in Eq. 1 as

$$\boldsymbol{F} = \underbrace{\boldsymbol{F}_e \, \boldsymbol{R}_g}_{:=\boldsymbol{F}_*} \boldsymbol{U}_g = \boldsymbol{F}_* \, \boldsymbol{U}_g. \tag{3}$$

The right Cauchy-Green tensor associated with the mapping $\boldsymbol{F}_*$ shall then be

$$\boldsymbol{C}_* = \boldsymbol{F}_*^T \, \boldsymbol{F}_* = \boldsymbol{U}_g^{-1} \, \boldsymbol{C} \, \boldsymbol{U}_g^{-1}. \tag{4}$$

The Helmholtz free energy per unit volume in the reference configuration is additively split into an isotropic part associated with the isotropic ground matrix, and an anisotropic part corresponding to the collagen fibres, i.e.,

$$\psi = \psi_{\mathsf{iso}} + \psi_{\mathsf{ani}}. \tag{5}$$

With $\boldsymbol{U}_g$ as an internal variable, the Helmholtz free energy for the isotropic ground matrix, encompassing the behaviors of the smooth muscle cells, elastins, and proteoglycans, is prescribed to be of the Neo-Hookean form as

$$\psi_{\mathsf{iso}}(\boldsymbol{C}, \boldsymbol{U}_g) = \frac{\mu}{2} \left(\mathrm{tr} \, \boldsymbol{C}_* - 3 \right) - \mu \ln J_* + \frac{\Lambda}{4} \left(J_*^2 - 1 - 2 \ln J_* \right), \tag{6}$$

where $J_* = \sqrt{\mathsf{det}(\boldsymbol{C}_*)}$. We herein embed the directionality of the helices of collagen fibres via the generalized structural tensor approach [15], defining them to be of the form

$$\boldsymbol{H}_i \;\; = \;\; \kappa \, \boldsymbol{I} + (1 - 3\,\kappa) \; \boldsymbol{a}_{0i} \otimes \boldsymbol{a}_{0i} \tag{7}$$

for each helix ($i = 1, 2$). Here κ refers to the dispersion parameter, and $\boldsymbol{a}_{0i}$ to the collagen orientations in the reference configuration. The Helmholtz free energy associated with the collagen fibres is then chosen to be of the form

$$\psi_{\mathsf{ani}}(\boldsymbol{C}, \boldsymbol{H}_1, \boldsymbol{H}_2, c_{_C}^0) = \frac{k_1}{2k_2} \sum_{i=1,2} \left(\mathsf{exp} \left[k_2 \langle E_i \rangle^2 \right] - 1 \right), \tag{8}$$

where

$$E_i := \boldsymbol{H}_i : \boldsymbol{C} - 1, \tag{9}$$

and the stress-like parameter k_1 is scaled according to the local collagen concentration in the reference configuration ($c_{_C}^0$), i.e.,

$$k_1 = \bar{k}_1 \left(\frac{c_{_C}^0}{c_{_{C,eq}}} \right), \tag{10}$$

where $\bar{k}_1$ is the stress-like material parameter for healthy collagen and $c_{_{C,eq}}$ is the homeostatic collagen concentration in a healthy artery.

Volumetric growth is achieved via the direct prescription of the growth stretch tensor $\boldsymbol{U}_g$ [16] based on the amount of dispersion κ, which can be histologically inferred. Two forms are proposed herein, namely,

$$\begin{aligned} (\kappa \approx 0) \quad &: \qquad \boldsymbol{U}_g := \boldsymbol{I} + (\vartheta - 1) \, \boldsymbol{\gamma} \otimes \boldsymbol{\gamma}, \quad \boldsymbol{\gamma} := \frac{\boldsymbol{a}_{01} \times \boldsymbol{a}_{02}}{||\boldsymbol{a}_{01} \times \boldsymbol{a}_{02}||}, \quad \vartheta := \frac{\rho_{_S}^0}{\rho_{_{S,eq}}} \\ (\kappa > 0) \quad &: \qquad \boldsymbol{U}_g := \vartheta \, \boldsymbol{I}, \quad \vartheta := \left(\frac{\rho_{_S}^0}{\rho_{_{S,eq}}} \right)^{1/3}, \end{aligned} \tag{11}$$

where $\rho_{_S}^0$ is the local SMC density in the reference configuration, and $\rho_{_{S,eq}}^0$ is the SMC density in a healthy homeostatic vessel.

2.2 Balance equations

The balance equations for the concentrations of PDGF ($c_{_P}$), TGF-β ($c_{_T}$), ECM with collagen as the primary constituent ($c_{_C}$), and the drug ($c_{_D}$), in addition to the densities of SMCs ($\rho_{_S}$) and ECs ($\rho_{_E}$) are set up to model the chemo-biological interactions involved in neointimal hyperplasia. The advection-reaction-diffusion equation forms the basis for the aforementioned balance of mediators, the general form of which in the Eulerian description is

$$\underbrace{\left.\frac{\partial \phi}{\partial t}\right|_{\boldsymbol{x}}}_{\text{rate}} + \underbrace{\operatorname{div}(\phi\,\boldsymbol{v})}_{\text{advection}} = \underbrace{\operatorname{div}(k\,\operatorname{grad}\phi)}_{\text{diffusion}} + \underbrace{\overset{\text{source}}{\mathcal{R}} - \overset{\text{sink}}{\mathcal{S}}}_{\text{reaction}}. \tag{12}$$

The particularized balance equations for the mediators are set up based on the physiological response of a stented artery in an inflammatory setting and are summarized to be

PDGF :

$$\left.\frac{\partial c_{_P}}{\partial t}\right|_{\boldsymbol{x}} + \operatorname{div}(c_{_P}\,\boldsymbol{v}) = \underbrace{\operatorname{div}(D_{_P}\,\operatorname{grad} c_{_P})}_{\text{diffusion}} + \underbrace{\big((1-r_{_\eta}) + r_{_\eta}\,f_{P1}(c_{_D})\big)\,\eta_{_P}\rho_{_S}\,c_{_T}}_{\substack{\text{secretion by SMCs}\\ \text{and macrophages}}} - \underbrace{\varepsilon_{_P}\,f_{P2}(c_{_T})\,\rho_{_S}\,c_{_P}}_{\substack{\text{receptor}\\ \text{internalization}}}, \tag{13}$$

TGF-$\boldsymbol{\beta}$:

$$\left.\frac{\partial c_{_T}}{\partial t}\right|_{\boldsymbol{x}} + \operatorname{div}(c_{_T}\,\boldsymbol{v}) = \underbrace{\operatorname{div}(D_{_T}\,\operatorname{grad} c_{_T})}_{\text{diffusion}} - \underbrace{\varepsilon_{_T}\,\rho_{_S}\,c_{_T}}_{\substack{\text{receptor}\\ \text{internalization}}}, \tag{14}$$

ECM :

$$\left.\frac{\partial c_{_C}}{\partial t}\right|_{\boldsymbol{x}} + \operatorname{div}(c_{_C}\,\boldsymbol{v}) = \underbrace{\eta_{_C}\rho_{_S}\left(1-\frac{c_{_C}}{c_{_{C,th}}}\right)}_{\substack{\text{secretion by}\\ \text{synthetic SMCs}}} - \underbrace{\varepsilon_{_C}\,c_{_P}\,c_{_C}}_{\substack{\text{MMP-induced}\\ \text{degradation}}}, \tag{15}$$

drug (rapamycin):

$$\left.\frac{\partial c_{_D}}{\partial t}\right|_{\boldsymbol{x}} + \operatorname{div}(c_{_D}\,\boldsymbol{v}) = \underbrace{\operatorname{div}(D_{_D}\,\operatorname{grad} c_{_D})}_{\text{diffusion}} - \underbrace{\varepsilon_{_{D1}}\,\rho_{_S}\,c_{_D}}_{\substack{\text{receptor}\\ \text{internalization}}}, \tag{16}$$

EC :

$$\left.\frac{\partial \rho_{_E}}{\partial t}\right|_{\boldsymbol{x}} + \operatorname{div}_{\Gamma}(\rho_{_E}\,\boldsymbol{v}_{\Gamma}) = \operatorname{div}_{\Gamma}\left(D_{_E}\,\operatorname{grad}_{\Gamma}\rho_{_E}\right) + \underbrace{\eta_{_E}\,f_{E1}(c_{_D})\,\rho_{_E}\left(1-\frac{\rho_{_E}}{\rho_{_{E,eq}}}\right)}_{\text{proliferation}} - \underbrace{\varepsilon_{_E}\,f_{E2}(c_{_D})\,\rho_{_E}}_{\text{apoptosis}}, \tag{17}$$

SMC :

$$\left.\frac{\partial \rho_{_S}}{\partial t}\right|_{\boldsymbol{x}} + \mathsf{div}\,(\rho_{_S}\,\boldsymbol{v}) = \underbrace{-\,\mathsf{div}\left(\rho_{_S}\,\overbrace{\chi_{_{S1}}\left(1-\frac{c_{_C}}{c_{_{C,th}}}\right)\,\mathsf{grad}\,c_{_P}}^{\boldsymbol{v}_{_{S1}}}\right)}_{\text{chemotaxis}} + \underbrace{\mathsf{div}\left(\rho_{_S}\,\overbrace{\chi_{_{S2}}\,f_{_{S1}}(c_{_P})\,\mathsf{grad}\,c_{_C}}^{-\boldsymbol{v}_{_{S2}}}\right)}_{\text{haptotaxis}}$$
$$\underbrace{+\,\eta_{_S}\,f_{_{S2}}(c_{_P})\,f_{_{S3}}(c_{_T})\,f_{_{S4}}(c_{_D})\,\rho_{_S}\left(1-\frac{c_{_C}}{c_{_{C,th}}}\right)}_{\text{proliferation}}, \tag{18}$$

the scaling functions embedded in the above balance equations being defined to be

$$f_{_{P1}}(c_{_D}) := \exp(-l_{_{P1}}\,c_{_D}) \in [0,1], \tag{19}$$

$$f_{_{P2}}(c_{_T}) := \frac{1}{1+\exp\left(l_{_{P2}}\left(c_{_T}-c_{_{T,th}}\right)\right)} \in [0,1] \tag{20}$$

$$f_{_{S1}}(c_{_P}) := \frac{1}{1+\exp\left(-l_{_{S1}}\left(c_{_P}-c_{_{P,th}}\right)\right)} \in [0,1] \tag{21}$$

$$f_{_{S2}}(c_{_P}) := 1-\exp(-l_{_{S2}}\,c_{_P}) \in [0,1], \tag{22}$$

$$f_{_{S3}}(c_{_T}) := \frac{1}{1+\exp\left(l_{_{S3}}\left(c_{_T}-c_{_{T,th}}\right)\right)} \in [0,1], \tag{23}$$

$$f_{_{S4}}(c_{_D}) := 1-\frac{1}{100}\left(\frac{A_{_S}\,c_{_D}^{\alpha}}{c_{_D}^{\alpha}+B_{_S}^{\alpha}}\right), \tag{24}$$

$$f_{_{E1}}(c_{_D}) := 1-\frac{1}{100}\left(\frac{A_{_E}\,c_{_D}^{\beta}}{c_{_D}^{\beta}+B_{_E}^{\beta}}\right), \tag{25}$$

$$f_{_{E2}}(c_D) := 1-\exp(-l_{_E}\,c_{_D}) \in [0,1], \tag{26}$$

and $\boldsymbol{v}_{_{S1}}$ and $\boldsymbol{v}_{_{S2}}$ referring to the chemotactic and haptotactic velocities respectively. It is to be mentioned here that all the equations for the mediators except that for the ECs are solved in the bulk domain of the arterial wall, while that for the ECs is solved only on the luminal surface. Hence the usage of the surface gradient and divergence operators in the balance equation for EC density. We herein employ the Lagrangian equivalent of the general form in Eq. 12, which is obtained from the transformation of the terms involved, given by

$$J^{-1}\,\dot{\phi^0} = J^{-1}\mathsf{Div}\left[k\,\boldsymbol{C}^{-1}\left(\mathsf{Grad}(\phi^0)-\left(\frac{\phi^0}{J}\right)\,\mathsf{Grad}\,J\right)\right]+\mathcal{R}_0-\mathcal{S}_0. \tag{27}$$

The quasi-static balance of linear momentum

$$\mathsf{Div}\,(\boldsymbol{F}\,\boldsymbol{S})+\boldsymbol{B}=\boldsymbol{0}, \tag{28}$$

forms the basis for modeling the structural response of the arterial wall, $\boldsymbol{S}$ being the second Piola-Kirchhoff stress tensor, and $\boldsymbol{B}$ the body force vector in the reference configuration. The inertial effects of the added mass that results in the slow growth process are hence ignored.

3 Numerical examples

The weak forms in the Lagrangian coordinates of the equations set up in the previous section are spatially discretized with trilinear hexahedral elements for the bulk of the arterial wall and bilinear quadrilateral elements for the luminal surface. Temporal discretization is obtained via the backward-Euler method. The framework is then implemented in the commercial finite element package *FEAP* via user-defined elements. The parameters involved are either extracted from literature or when not available, choices that result in physiological macroscopic outcomes are incorporated. Two initial boundary value problems (IBVPs) are investigated using the framework.

3.1 Quadrant of a simplified stented artery

One quadrant of a cylindrical section of an artery, as shown in Fig. 1 (left), is contrived to test the modeling framework. Part of the luminal surface (in blue) is considered denuded due to stent implantation, upon which flux (inhomogeneous Neumann) boundary conditions ($\bar{q}_P$ and $\bar{q}_T$) are applied for the PDGF and TGF-β fields replicating the platelet activation process.

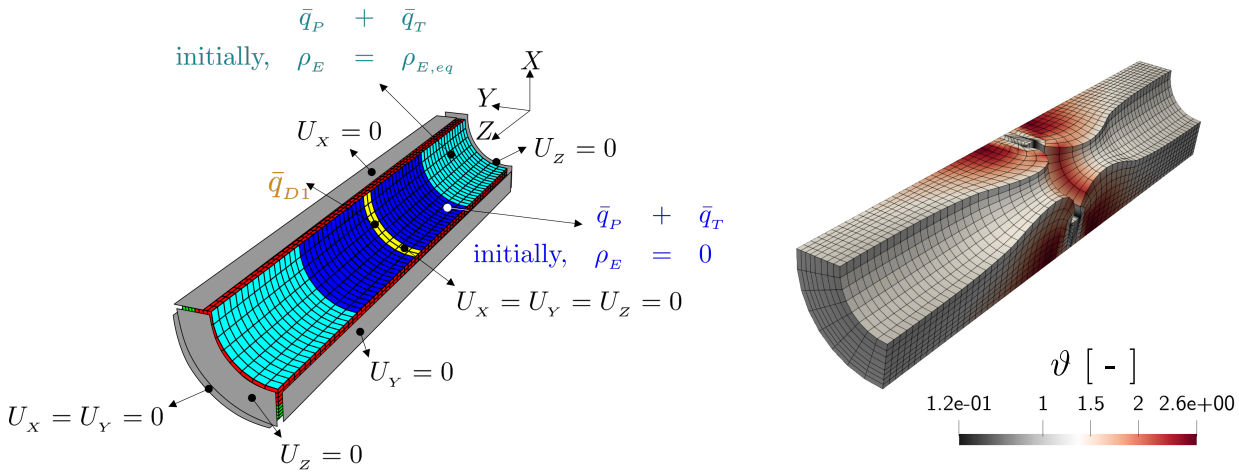

Figure 1: left - IBVP setup; right - growth stretch contour

An idealized cylindrical stent is assumed to be implanted within the artery, the effect of which is captured by fixing the structure against all displacements at the region of stent apposition (in yellow), while applying flux boundary conditions on the aforementioned region to model the drug-elution. Symmetry is utilized along the circumferential-longitudinal plane. The rest of the displacement boundary conditions serve to arrest rigid body movements. The IBVP hence set up is utilized to evaluate the effect of the drug release rate, that result in the cumulative release profiles as shown in Fig. 2 (left), on the severity of neointimal hyperplasia 1 [year] after stent insertion. It is observed that at a predefined level of drug embedment in the drug-eluting stent struts, a slower release of the drug shall result in the least amount of restenotic growth (see Fig. 2 (right)).

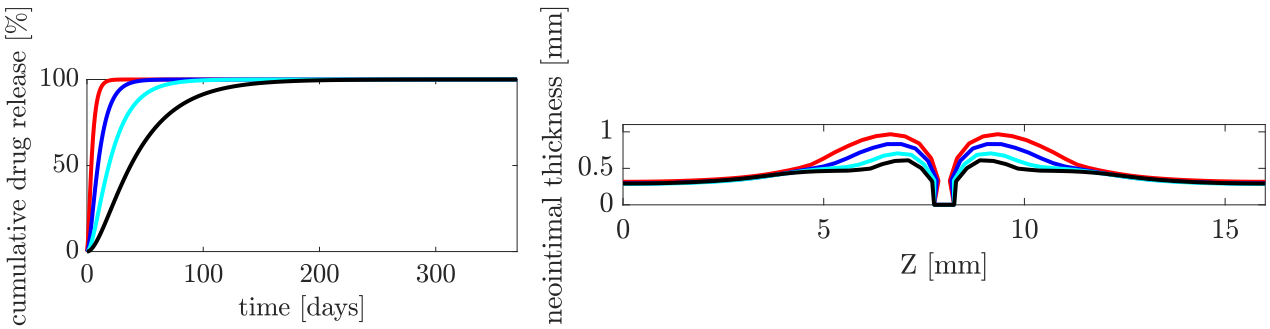

Figure 2: left - cumulative drug release profiles; right - neointima profiles after 1 [year]

3.2 XIENCE-V stent

To test the applicability of the modeling framework in a complex geometric setting, a segment of the human coronary artery implanted with a XIENCE-V stent (Abbott Vascular Inc.) is considered. Γ_E^d is the region where the endothelium is assumed to be fully denuded due to the stent implantation procedure. Therefore, EC density ρ_E is initialized to be zero at this region. Along the annular edges of the luminal surface (Γ_E^h) EC density is initialized to be equal to the healthy homeostatic value to initiate the endothelial recovery process. Γ_{SS} is the stent apposition region on the luminal side where the drug influx is prescribed. The longitudinal end surfaces are constrained against longitudinal displacements while the abluminal cylindrical surfaces are constrained against radial displacements. The stent apposition region is fixed against all displacements.

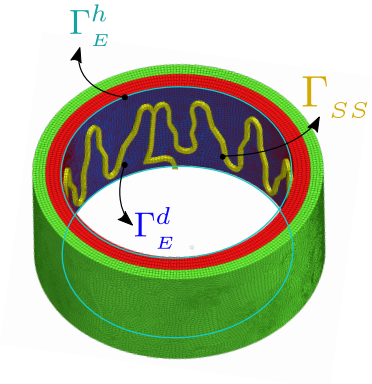

Figure 3: XIENCE-V stent in a coronary artery

A period of 120 [days] is simulated using the model hence set up. Fig. 4 depicts the endothelial recovery process after the implantation of a bare-metal XIENCE-V stent. Partial reendothelialization is observed to occur fairly quickly. But the slow process of fully functional reendothelialization leads to a large accumulation of growth factors in the subintimal space leading to an exacerbated growth response. The absence of the drug contributes to intense growth since no anti-inflammatory effects are present within the arterial wall in this case.

As can be seen in Fig. 5, the level of drug embedded in the stent struts, controlled via the peak drug influx parameter $\bar{q}_D^{\mathsf{ref}}$ highly influences the restenotic growth since the healing of the endothelium is delayed in the presence of rapamycin. Additionally, it points to the existence

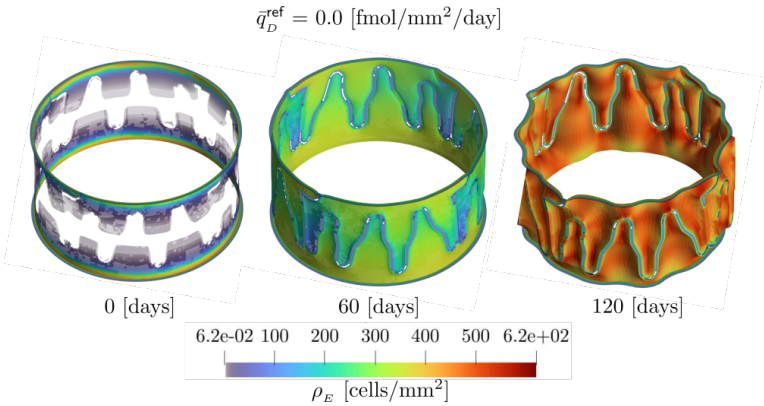

Figure 4: endothelial recovery in the absence of the drug

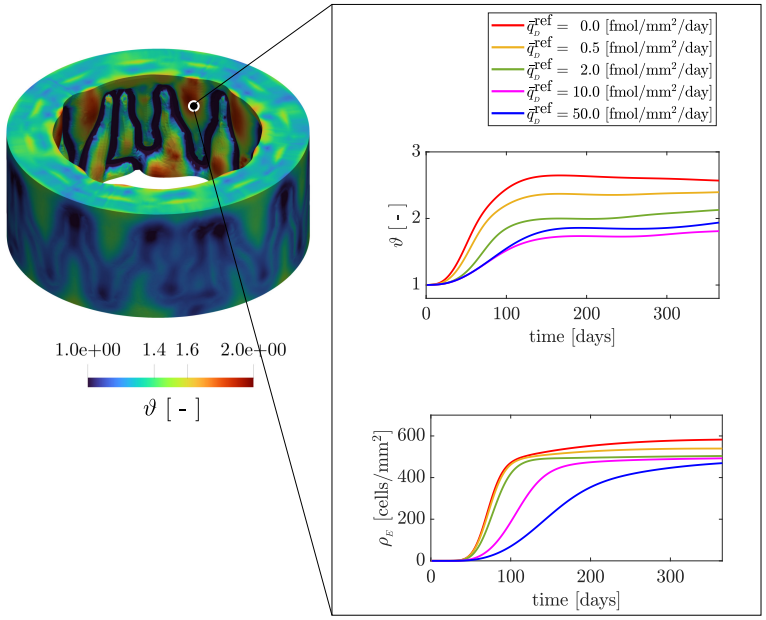

Figure 5: growth stretch evolution and endothelial recovery for varying drug embedment levels

of an optimal level of drug embedment ($\bar{q}_D^{\text{ref}} = 10$ [fmol/mm^2/day]) which leads to minimal neointima formation reflected in the values of the growth stretch ϑ.

4 Accelerated and versatile computations

4.1 Finite element technologies

Special solid-shell [17] and solid-beam [18] finite element formulations with reduced integration and hourglass stabilization have been developed in the group to simulate slender structures efficiently. These formulations are capable of treating volumetric and shear locking. One structural example is modeling textile-reinforced heart valves. As shown in Fig. 6, the structure can be computed using only one element through the thickness direction, each containing three Gauss points. This allows us to perform the computations with a significantly lower element count. Furthermore, in case of reduced integration, the material model is evaluated at fewer Gauss points, substantially reducing the computational cost.

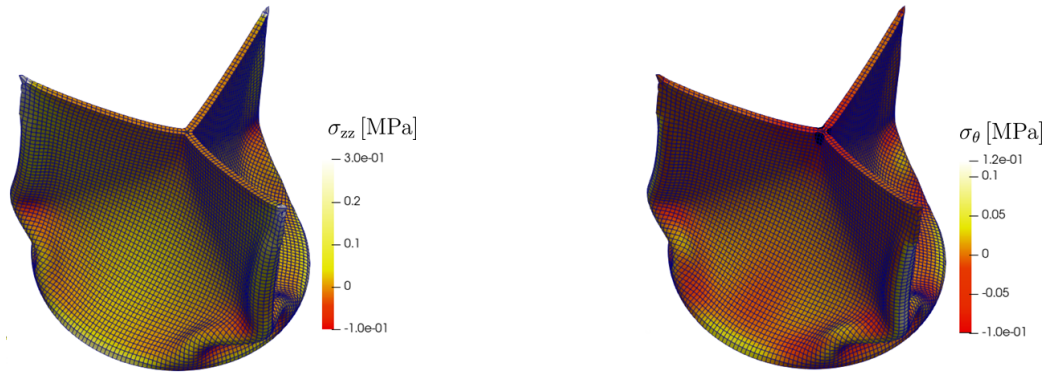

(a) (b)

Figure 6: Cauchy stress contour for heart valve at its closed position. (a) Stress along the longitudinal direction and (b) stress along the circumferential direction.

4.2 Physics-informed neural networks

As an alternative strategy, the coupled PDEs addressing the underlying biological system were solved using physics-informed neural networks (PINNs). Note that the mechanical displacement fields and related quantities (e.g. free energy functional, stresses, and strains) were not coupled in the current biological PINNs. The constitutive growth modeling associated with the mechanical part can be implemented independently by incorporating the SMC density, which is computed from current PINNs, as an input parameter.

The network structure incorporates six hidden layers with 80 nodes each and a total of 200 000 domain points, 50 000 boundary points, and 50 000 initial points. The input nodes include the space and time coordinates and the output nodes are the mediators. The activation function used is the hyperbolic tangent (tanh), and the Glorot uniform initializer is applied. A learning rate of 1.0×10^{-3} is employed, with a maximum of 20 000 iterations using the Adam optimizer. The training is performed using the TensorFlow 2.x backend on the RWTH Aachen cluster workstation. The total loss function defined in the training process is based on the sum of mean squared errors (MSE) of various terms, including governing PDEs, initial conditions, Dirichlet boundary conditions, and Neumann boundary conditions, which is plotted in Fig. 7.

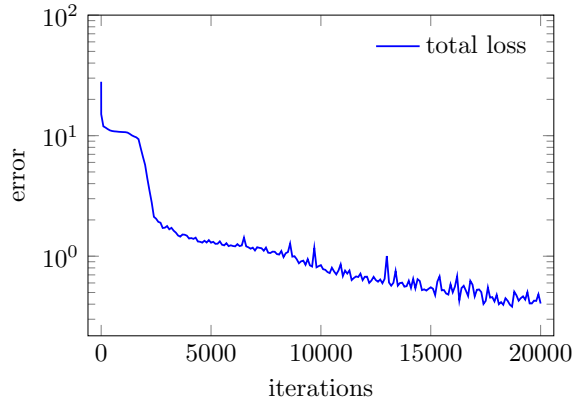

Figure 7: Error-iteration diagram.

Figs. 8 and 9 illustrate the results of both PINNs and FEM concerning the drug concentration and SMC density 180 days after PCI. The comparison indicates that the results obtained from both solvers exhibit consistency and only a slight difference can be observed for the drug concentration.

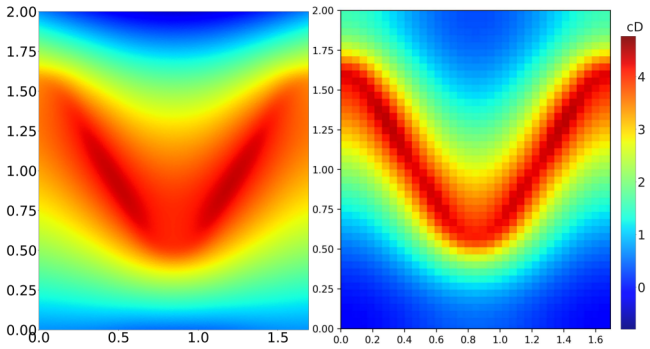

Figure 8: Drug concentration 180 [days] after PCI, computed by left: PINNs and right: in-house FEM.

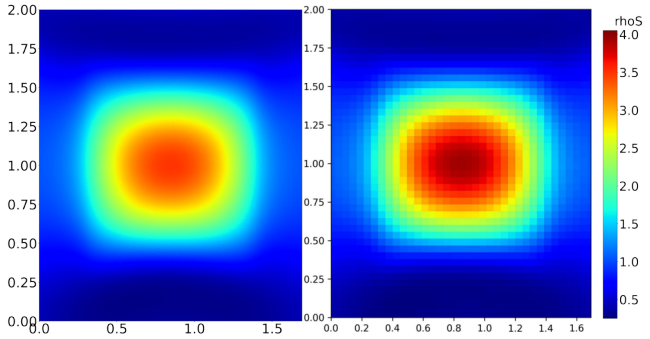

Figure 9: SMC density 180 [days] after PCI, computed by left: PINNs and right: in-house FEM.

Although the PINNs demonstrate success in solving coupled PDEs, it is observed that network training poses challenges and exhibits slower computational speed compared to FEM solvers, where the PINNs require a total memory of ≈ 120 Gbyte and a computational time of ≈ 3 days. FEM shows dramatic efficiency in saving memory and computational effort. This restriction of PINNs can be potentially solved by combining model order reduction (MOR) techniques and could be of great interest in the near future. Nevertheless, PINNs exhibit distinct advantages over finite element simulation methods due to their meshless nature and flexibility in accommodating variations in material properties, domain, and boundary conditions with ease.

5 Conclusion and outlook

A multiphysics modeling framework is presented herein that captures the intricate mechanisms involved in ISR and the counteracting effects intended with the embedment of drugs in current-generation DESs. The model exposes the need for the optimization of the level of drug embedment as well as the rate of drug release patient-specifically. With the implementation of

the finite element technologies discussed, an acceleration in the computational time is intended. Further, through the usage of PINNs as the solver PDEs, and with sufficient computational infrastructure, real-time patient-specific simulations are foreseen to be achieved, thereby bridging the gap between computational tools and clinical practice.

6 Acknowledgements

This work has been funded through the financial support of the German Research Foundation (DFG) for the projects: (a) "Drug-eluting coronary stents in stenosed arteries: medical investigation and computational modelling" (project number 395712048: RE 1057/44-1, RE 1057/44-2), (b) "In-stent restenosis in coronary arteries - in silico investigations based on patient-specific data and meta modeling" (project number 465213526: RE 1057/53-1), a subproject of "SPP 2311: Robust coupling of continuum-biomechanical in silico models to establish active biological system models for later use in clinical applications - Co-design of modeling, numerics and usability", and (c) "Modelling of Structure and Fluid-Structure Interaction during Tissue Maturation in Biohybrid Heart Valves", a subproject of "PAK961 - Modeling of the structure and fluid–structure interaction of biohybrid heart valves on tissue maturation" (project number 403471716: RE 1057/45-1, RE 1057/45-2), which is gratefully acknowledged.

REFERENCES

[1] Evans, D. J., Lawford, P. V., Gunn, J., Walker, D., Hose, D. R., Smallwood, R. H., Chopard, B., Krafczyk, M., Bernsdorf, J., and Hoekstra, A. (2008). *The application of multiscale modelling to the process of development and prevention of stenosis in a stented coronary artery.* Philosophical transactions. Series A, Mathematical, physical, and engineering sciences, 366(1879), 3343–3360.

[2] Tahir, H., Hoekstra, A. G., Lorenz, E., Lawford, P. V., Hose, D. R., Gunn, J., and Evans, D. J. (2011). *Multi-scale simulations of the dynamics of in-stent restenosis: impact of stent deployment and design.* Interface focus, 1(3), 365–373.

[3] Zahedmanesh, H., Van Oosterwyck, H., and Lally, C. (2014). *A multi-scale mechanobiological model of in-stent restenosis: deciphering the role of matrix metalloproteinase and extracellular matrix changes.* Computer methods in biomechanics and biomedical engineering, 17(8), 813–828.

[4] Zun, P., Svitenkov, A., and Hoekstra, A. (2021). *Effects of local coronary blood flow dynamics on the predictions of a model of in-stent restenosis.* Journal of biomechanics, 120, 110361.

[5] Garikipati, K.C., Arruda, E.M., Grosh, K., Narayanan, H., and Calve, S. (2003). *A continuum treatment of growth in biological tissue: the coupling of mass transport and mechanics.* Journal of The Mechanics and Physics of Solids, 52, 1595-1625.

[6] Fereidoonnezhad, B., Naghdabadi, R., and Holzapfel, G. A. (2016). *Stress softening and permanent deformation in human aortas: Continuum and computational modeling with application to arterial clamping.* Journal of the mechanical behavior of biomedical materials, 61, 600–616.

[7] He, R., Zhao, L., Silberschmidt, V. V., and Liu, Y. (2020). *Mechanistic evaluation of long-term in-stent restenosis based on models of tissue damage and growth*. Biomechanics and modeling in mechanobiology, 19(5), 1425–1446.

[8] Budu-Grajdeanu, P., Schugart, R. C., Friedman, A., Valentine, C., Agarwal, A. K., and Rovin, B. H. (2008). *A mathematical model of venous neointimal hyperplasia formation*. Theoretical biology & medical modelling, 5, 2.

[9] Escuer, J., Martínez, M. A., McGinty, S., and Peña, E. (2019). *Mathematical modelling of the restenosis process after stent implantation*. Journal of the Royal Society, Interface, 16(157), 20190313.

[10] Caiazzo, A., Evans, D., Falcone, J-L., Hegewald, J., Lorenz, E., Stahl, B., Wang, D., Bernsdorf, J., Chopard, B., Gunn, J., Hose, D., Krafczyk, M., Lawford, P., Smallwood, R., Walker, D., and Hoekstra, A. (2011). *A Complex Automata approach for in-stent restenosis: Two-dimensional multiscale modelling and simulations*. J. Comput. Science. 2.

[11] Rossi, F., Casalini, T., Raffa, E., Masi, M., and Perale, G. (2012). *Bioresorbable polymer coated drug eluting stent: a model study*. Molecular pharmaceutics, 9(7), 1898–1910.

[12] McQueen, A., Escuer, J., Schmidt, A. F., Aggarwal, A., Kennedy, S., McCormick, C., Oldroyd, K., and McGinty, S. (2022). *An intricate interplay between stent drug dose and release rate dictates arterial restenosis*. Journal of controlled release: official journal of the Controlled Release Society, 349, 992–1008.

[13] Rodriguez, E. K., Hoger, A., and McCulloch, A. D. (1994). *Stress-dependent finite growth in soft elastic tissues*. Journal of biomechanics, 27(4), 455–467.

[14] Holthusen, H., Rothkranz, C., Lamm, L., Brepols, T., and Reese, S. (2022). *Inelastic material formulations based on a co-rotated intermediate configuration—Application to bioengineered tissues*. Journal of the Mechanics and Physics of Solids. 172. 105174.

[15] Gasser, T.C., Ogden, R.W., and Holzapfel, G.A. (2006). *Hyperelastic modelling of arterial layers with distributed collagen fibre orientations*. Journal of The Royal Society Interface, 3, 15 - 35.

[16] Lubarda, V.A., and Hoger, A. (2002). *On the mechanics of solids with a growing mass*. International Journal of Solids and Structures, 39, 4627-4664.

[17] Schwarze, M., and Reese, S. A reduced integration solid-shell finite element based on the EAS and the ANS concept—Large deformation problems. *International Journal for Numerical Methods in Engineering* (2011) 85(3):289-329.

[18] Frischkorn, J., and S. Reese. A solid-beam finite element and non-linear constitutive modelling. *Computer Methods in Applied Mechanics and Engineering* (2013) 265(3):195-212.